RSC Advances

ROYAL SOCIETY OF CHEMISTRY

www.rsc.org/advances

Band structure engineering of monolayer MoS_2: A charge compensated codoping strategy

Hui Wan[1], Liang Xu[1], Wei-Qing Huang[1*], Jia-Hui Zhou[1],Chao-Ni He [1], Xiaofan Li[1‡], Gui-Fang Huang[1#], P. Peng[2], Zheng-Gui Zhou[1]

[1] Department of Applied Physics, School of Physics and Electronics, Hunan University, Changsha 410082, China

[2] School of Materials Science and Engineering, Hunan University, Changsha 410082, China

Abstract:

The monolayer MoS_2, possessing an advantage over graphene in that it exhibits a band gap whose magnitude is appropriate for solar applications, has attracted increasing attention because of its possible use as photocatalysts. Herein, we propose a codoping strategy to tune the band structure of monolayer MoS_2 aimed at enhancing its photocatalytic activity using first-principles calculation. The monodoping (halogen element, Nd) introduces impurity states in the gap, thus decreasing the photocatalytic activity of MoS_2. Interestingly, the $Nb_{Mo}F_S$ codoping reduces the energy cost of doping as a consequence of the charge compensation between the niobium (p-dopant) and the fluorine (n-dopant) impurities, which eliminates the isolated levels (induced by monodopant) in the band gap. Most importantly, the $Nb_{Mo}F_S$ codoped MoS_2 has more active sites for photocatalysis. These results show the proposed $Nb_{Mo}F_S$ codoped monolayer MoS_2 is a promising photocatalyst or photosensitizers for visible light in the heterogeneous semiconductor systems.

*. Corresponding author. *E-mail address:* wqhuang@hnu.edu.cn, wqhuang2000@yahoo.com

‡. Corresponding author. *E-mail address:* yueyanglxf@hnu.edu.cn

#. Corresponding author. *E-mail address:* gfhuang@hnu.edu.cn

1. Introduction

Two-dimensional nanomaterials, such as graphene with unusual optical and electrical properties, have recently attracted a growing interest by virtue of their potential applications [1-8]. In particular, a multitude of electronic states have recently been observed in the layered transition metal dichalcogenides, making them as the ideal platforms for a quantity of applications [9, 10]. The monolayer MoS_2 (1H-MoS_2), a ‘‘layered’’ transition metal dichalcogenide semiconductor, being widely explored as catalyst [11], lubricant [12], and lithium ion battery anode [13], is a paradigm in this respect.

MoS_2 is formed by a graphene-like hexagonal arrangement of Mo and S atoms stacked together to give S-Mo-S sandwiches which are bonded together by weak Van-der-Waals forces [14] and coordinated in a triangular prismatic fashion. The electronic properties of bulk MoS_2 show a strong dependence on the layer thickness [15-17]. In this context, 1H-MoS_2, one kind of transition-metal dichalcogenides, is of particular interest [17-25]. Recently, two-dimensional (2D) 1H-MoS_2 has been successfully synthesized [26-28], displaying unique properties. These findings have triggered many theoretical studies [29-36] to tune its properties, such as decorating the pristine surface with adatoms or molecules to tune the electronic structure (also add catalytic sites) of 1H-MoS_2. Among them, the photocatalytic performance of MoS_2 has drawn particular attention due to its large surface area and catalytically active sites. Of critical importance, the band gap around 2.0 eV of MoS_2 is preferable in order to utilize the maximum portion of the solar visible light, thus making it to be a promising catalyst in various fields including hydrodesulfurization (HDS), hydrogen evolution reaction (HER), hydrogen generation and photocatalytic degradation of organic pollutants [37, 38]. It is found that the catalytic activity of MoS_2 plates is derived from the under coordinated sulfur edge sites, while their basal planes remain catalytically inert. Moreover, because of its layered nature and high surface energy of the two-dimensional structure, MoS_2 nanomaterials are prone to stacking together through π-π interaction during the preparation process, making a substantial amount of catalytic edge sites on MoS_2 blocked, and delivering higher resistance for the electron transfer and diffusion of reactant molecules, and retarding the

catalytic reaction. Therefore, the effective strategy to enhance the photocatalytic performance of MoS_2 by increasing edge catalytic sites or making their basal planes to be catalytic active is being actively pursued.

Introducing a small amount of foreign elements into the semiconductors with wide band gap is an effective method frequently used. For example, Komsa et al. [39] demonstrated the vacancy formation in 1H-MoS_2 and then the filling of vacancies with substitutional impurity atoms, verifying the above expectation and appears to be a promising way to extend the applications of MoS_2. Actually, the doping strategy has been widely used in many other systems, such as, N-doped Cu_2O [40], graphene [41], boron nitride [42] and related structures [43]. There are so far many reports available on specific dopants for 1H-MoS_2 [44-47]. However, it should be pointed out that some major issues may arise from monodoping. It has widely been recognized that monodoping of semiconductors with other elements produces localized electronic midgap states associated with dopants, which is the main reason of deteriorating their properties, such as photocatalytic properties. For examples, these localized states can boost electron-hole recombination, thereby diminishing the photocatalytic efficiency. Another key issue, particularly in the case of charge imbalance, is the formation of vacancies, which are efficient charge carrier traps. To overcome these problems, we employ the codoping strategy, which has been found to be very successful in modifying the band structure of semiconductor photocatalysts [48-50]. However, there are few studies reporting the significance of codoping in improving the photoactivity of 1H-MoS_2.

In this work, we propose, for the first time, the charge compensated codoping of Nd and F to modify the band structure of 1H-MoS_2. Basically, the introduction of Nd ($4s^2\ 4p^6\ 4d^4\ 5s^1$) atom in place of Mo ($4s^2\ 4p^6\ 4d^5\ 5s^1$) atom leads to one electron deficiency, which can be compensated by replacing one S ($3s^2\ 3p^4$) by F ($2s^2\ 3p^5$). Being very similar in atomic size, Nd can be easily fitted into the Mo lattice site without any large distortion in the crystal structure. Another reason for choosing Nd is due to that the Nd-doped 1H-MoS_2 has been prepared successfully by vapor-phase reaction [51]. We perform a detailed systematic calculation exploring the role of the codoping and individual dopant elements, as well as halogen element in place of S atom for comparison using density functional theory, which is a very popular tool for describing the electronic structures of

semiconductor materials. It is found that monodoping will cause acceptor or donor levels in the gap region. The charge compensated dopants, Nd and F, exhibit strong interactions through significant lattice relaxation. The stability of the codoped system has been assessed by calculating the defect-pair binding energy. Because the impurity levels are passivated, they will not be effective as carrier recombination centers. Furthermore, the $Nb_{Mo}F_S$-1H-MoS_2 has more active sites for photocatalytic reaction. This work is an example of heteroatom substitution in the case of 1H-MoS_2, opening up a wide range of possibilities including varying the electronic and optical behaviors of the monolayer MoS_2, in catalysis and in solar cells.

2. Theoretical model and computational details

The calculated crystal structure of 1H-MoS_2 belongs to the hexagonal system with the lattice constant a=b=3.160Å, c=12.295Å, the angle α=β=90°, γ =120°, and space group P63/mmc (194), as shown in Fig. 1. It is well known that 1H-MoS_2 consists of a monatomic Mo-layer between two monatomic S-layers like a sandwich structure (Fig. 1 (c) and (d)). Mo and S atoms alternatively occupy corners of a hexagon. A (3×3) hexagonal supercell (Fig. 1 (a)) with (9.48×9.48) $Å^2$ lateral dimensions is constructed and doping is introduced by replacing a single atom in the supercell, which contains 32 S and 16 Mo atoms. The two types of impurity atoms are introduced into the supercell by the modes of Nb_{Mo} (Nb atom substituting lattice Mo atom, Fig. 1 (a)) and NM_S (nonmetal atom substituting lattice S atom, NM=F, Cl, Br, and I, Fig. 1 (b)), resulting in five different kinds of doped MoS_2 models. In this work, $Nb_{Mo}F_S$-1H-MoS_2 is discussed as the typical representatives of codoping 1H-MoS_2 models. It should be pointed out that the doping metal atom (Nb) is to substitute Mo atom in the center of the (3×3) supercell, while the NM atom is to replace S atom which is the closest position to the substitutional atom. This is because that total energy calculations reveal that this kind of codoping atoms exhibit a strong tendency to form a pair occupying neighboring lattice sites.

The first-principles calculations are performed using density-function theory (DFT) as implemented in the CASTEP code [52]. The exchange-correlation interactions are treated by the generalized gradient approximation (GGA) with Perdew Burke Ernzerhof (PBE) functional [53], which are based on a total energy pseudo-potential plane wave method [54]. The vanderbilt ultrasoft pseudopotential is used to deal with the interaction between valence electrons and the

ionic core, and the valence atomic configurations are Mo: $4s^2\ 4p^6\ 4d^5\ 5s^1$, S: $3s^2\ 3p^4$, Nb: $4s^2\ 4p^6\ 4d^4\ 5s^1$, F: $2S^2\ 2p^5$, Cl: $3S^2\ 3p^5$, Br: $4S^2\ 4p^5$, and I: $5S^2\ 5p^5$, respectively. The cutoff energy is set to 400 eV, the *k*-point mesh of 9×9×1 and the self-consistent field (SCF) of 1×10^{-6} eV/atom is used for geometry optimizations using the Monk horst-Pack scheme [55]. Geometry optimization is carried out before single point energy calculation and the force on the atoms is less than 0.03 eV/Å, the stress on the atoms is less than 0.05 GPa, the atomic displacement is less than 1.0×10^{-3} eV/Å, and the energy change per atom is less than 1.0×10^{-5} eV. Periodic boundary conditions are applied and a vacuum layer of at least 10 Å is placed above the monolayer to minimize the interaction between the adjacent periodic images. To check the reliability of the results, a test calculation with higher plane-wave cutoff energy and more *k*-points is conducted. Compared with the cutoff energy of 400 eV, negligible changes are obtained for both structural and electronic structures and the difference between the total energies is less than 0.03 %. So the calculations in the present work are valid.

3. Results and discussion

3.1 Geometric Structures

To assess the accuracy of our computation method, we perform a series of calculations for 1H-MoS_2 supercell optimization. First, we implement structural optimization for pristine 1H-MoS_2. The equilibrium lattice constant after optimization is $a=b=3.18$ Å, which is in good agreement with the experimental value ($a=b=3.27$ [56] or 3.20 [57] Å), assuring the validity of the calculations. Consequently, the same calculation conditions are adopted to calculate the geometrical and electronic structures of the pure and doped 1H-MoS_2.

The changes in lattice parameters and bond lengths of doped 1H-MoS_2 are summarized in Table 1. One can see that the lattice constant change of Nb_{Mo}-1H-MoS_2 is the biggest of all. This is due to the length of Nb-S bond (2.455 Å) longer than that of Mo-S bond (2.409 Å) in pure 1H-MoS_2 because the electronegativity of Nb atom (1.6) is smaller than that of Mo atom (2.16), although the radius of Nb (1.45) and Mo (1.39) atoms have a few differences. For the NM_S-1H-MoS_2 case, the lattice constant changes are different with increasing their atomic numbers. The optimized lattice parameter of F_S-1H-MoS_2 is decreased, owing mainly to that the

larger electronegativity of F atom (3.98) leads to a shorter length of F-Mo bond (2.275 Å). While the lattice parameters of Cl_S-1H-MoS_2, Br_S-1H-MoS_2, and I_S-1H-MoS_2 are increased due to the Cl-Mo, Br-Mo, and I-Mo bond lengths elongating to 2.517, 2.671, and 2.897 Å, respectively, which can largely be attributed to the much bigger atomic radius of Cl (1.62 Å), Br (1.15 Å), and I (1.4 Å) than S (1.04 Å) atom. Interestingly, the lattice parameters of codoping 1H-MoS_2 have changed very little, only a reduction of 0.13% (9.530 Å vs 9.542 Å). Two important factors are responsible for the small change in the lattice parameters of codoping 1H-MoS_2. The first is the discrepancies in both the radius and the electronegativity of host atoms and substitutional atoms. The other factor directly impacting the lattice parameters of codoping 1H-MoS_2 is the coupling between the substitutional metal and nonmetal atoms.

To understand the charge redistribution induced by Nb or NM dopant, we calculate the electron density difference for the doped 1H-MoS_2 supercells, as shown in Fig. 2. The population of the selected atoms is also given by the numbers. The maps of pure phase are also plotted for comparison. It can be seen from parts (b) and (c) of Fig. 2 that when the Nb or F atom substitutes the lattice Mo or S atom, after charge redistribution, the interactions of Nb-S or Mo-F bond becomes stronger than the original Mo-S bonds, and the maps indicate that Nb atom lose charges and F atom withdraws charges from Mo atoms. Furthermore, Mulliken charge population analyses are calculated and listed in Table 2. We can find some useful information from the relative values of Mulliken population. The Nb atom is deprived of 0.34 e, while the charge of F atom is -0.42 e, capturing from the adjacent Mo cations, which are much more than that on the Mo atom (0.05 e) and S atom (-0.02 e) in the pure phase. Thus, we contribute the stronger Nb-S and Mo-F bonds to the more charge transfer from adjacent atoms. The smaller interaction of Cl-Mo, Br-Mo, and I-Mo (Fig. 2) is mainly due to the weak ability of Cl atom (-0.04 e) to withdraw charge, while Br and I atoms deprive charges by adjacent Mo atom. The dopant-dopant coupling is significant in the $Nb_{Mo}F_S$-1H-MoS_2, in which the substitutional Nb and F could form a strong Nb-F bond because F atom withdraws charges from Nb atom along with the direction of Nb-F bond, as shown in Fig. 2 (g).

3.2. Defect formation energy

The analysis on optimized geometry structure shows that the different dopants generate different lattice distortions, which makes the supercells of 1H-MoS_2 with various total energies. In order to examine the relative stability of the doped systems, the formation energies (ΔE_{form}) have been calculated according to the following equation:

$$\Delta E_{form} = E_{tot}(\alpha) - E_{tot}(MoS_2) - \sum n_A \mu_A + \sum n_B \mu_B$$

$$+q(E_{VBM} + \epsilon_F + \Delta V) \qquad (1)$$

where A=Nb, F, Cl, Br, or I, B=Mo or S. $E_{tot}(\alpha)$ is the total energy of the system including the substitutional atom A in the charge state q, $E_{tot}(MoS_2)$ is the total energy of the corresponding pristine 1H-MoS_2, while μ_A and μ_B are the chemical potentials of the substitutional atom A and of the substituted Mo (S) host atom, respectively. The chemical potentials of the A dopants are calculated with respect to bulk (A_2 dimers) reference levels for Mo (S) substitution. The electron chemical potential (i.e., the Fermi level), ϵ_F, is referenced to the valence-band maximum (VBM) of the bulk material, and the ΔV term is an extra shift in the average electrostatic potential which aligns the VBM of dopant supercells with bulk VBM. The formation energy of MoS_2 itself, $E_{form}(MoS_2)$, can be calculated from the expression

$$E_{form}(MoS_2) = \mu_{MoS_2} - \mu_{Mo} - 2\mu_S \qquad (2)$$

where μ_{MoS_2} is equal to $E_{tot}(MoS_2)$ per MoS_2 formula unit, and μ_{Mo} (μ_S) is the total energy per atom of Mo (S) in its reference phase. For Mo the reference phase used is the bulk metallic body-centered-cubic (bcc) structure, whereas for S it is the S_2 molecule (we note that the choice of reference phase is not unique). The value of $E_{form}(MoS_2)$ is then calculated to −2.84 eV in DFT-GGA which coincide with −2.88 eV [58].

The value of μ_B in Eq. (1), and therefore also E_{form}, largely depends on the experimental growth conditions. As limiting cases we consider the Mo-rich and S-rich situations. Under Mo-rich conditions the Mo chemical potential is equal to the bulk Mo value, $\mu_{Mo}^{Mo-rich} = \mu_{Mo}$. In thermodynamic equilibrium one can assume that $\mu_{MoS_2} = \mu_{Mo} + 2\mu_S$, so that for Mo-rich

conditions the S chemical potential is $\mu_S^{Mo-rich} = \frac{1}{2}(\mu_{MoS_2} - \mu_{Mo})$. Hence, by using Eq. (2), the chemical potentials for the Mo-rich limit can then be written as

$$\mu_{Mo}^{Mo-rich} = \mu_{Mo} \quad (3)$$

$$\mu_S^{Mo-rich} = \mu_S + \frac{1}{2}E_{form}[MoS_2] \quad (4)$$

Analogously, for S-rich conditions one obtains

$$\mu_{Mo}^{S-rich} = \mu_{Mo} + E_{form}[MoS_2] \quad (5)$$

$$\mu_S^{S-rich} = \mu_S \quad (6)$$

Table 3 lists the formation energies of all the impurities studied in this paper. Impurity formation energies in both S-rich and Mo-rich conditions, respectively, are shown in Fig. 3. As is known, the smaller defect formation energy is, the more preferable to incorporate impurity atoms into the host material. AS one halogen element NM occupies a sulfur site (NM_S), it can release an additional valence electron to the conduction band, thus causing NM_S to act as a donor. It can be observed from Table 3 (b) - (e)，the E_{form} gradually increase, and the defect formation energy of F_S is smaller than others. This is mainly due to the stronger interaction of F_S than Cl_S, Br_S, and I_S and the latter becomes smaller, indicating that F_S is easier to form. The results are similar with the previous study of F doped in MoS_2 [47]. In Fig. 3, the defect formation energy Nb_{Mo} has the lowest formation energy, suggesting a favorable replacement of Mo atom with Nb, which is in good agreement with previous calculations [20]. This can be interpreted by nearly the same radius of Mo and Nb atoms, indicating smaller distortion and fewer changes of the equilibrium structure and system energy. Interestingly, the defect formation energy of $Nb_{Mo}F_S$-1H-MoS_2 are smallest, no matter in S-rich or Mo-rich, manifesting that simultaneous substitutional Nb and F atom codoping is stable and more favored than F and Nb atom monodoping in 1H-MoS_2. Most importantly, the Nb and F is a charge-compensated donor-acceptor pair, which will be more favorable to enhance visible light photoactivity. We can see from Fig. 3 that all doped systems, except Nb_{Mo}, in S-rich conditions have higher formation energy than in Mo-rich conditions. This reflects the fact that the formation energy is largely dependent on the growth conditions. The large variation of the

formation energies for S substitutions in 1H-MoS_2 with respect to different values of μ_S has also been reported in Ref. [39]. The negative formation energies indicate the corresponding substitutional reactions could happen. Thus, the Nb_{Mo} and $Nb_{Mo}F_S$ doped 1H-MoS_2 are possible to be formed in the experiments.

3.3 Electronic structure

To investigate the effects of doping on the electronic properties, the band structures of pure 1H-MoS_2, Nb_{Mo}-1H-MoS_2, F_S-1H-MoS_2, Cl_S-1H-MoS_2, Br_S-1H-MoS_2, I_S-1H-MoS_2, and $Nb_{Mo}F_S$-1H-MoS_2 are calculated using DFT approach, which provides a reliable description of the ground state electronic structure. The calculated band structures, density of states (DOS) and projected density of states (PDOS) of the pure and doped 1H-MoS_2 are displayed in Figs. 4 and 5, respectively. The Fermi level is set at zero energy to easily identify the band gap and the relative position of the states from the impurity atoms. Based on the calculated band structures, the E_v (the energy for the top of VB), E_c (the energy for the bottom of conduction band (CB)), and E_g (the energy for the band gap) of the pure and doped 1H-MoS_2 are listed in Table 4.

As is shown in Fig. 4 (a), pure 1H-MoS_2 is a kind of direct band gap semiconductor, with the computed band gap of 1.652 eV, which agrees well with the MoS_2 photoluminescence experiment [17] and previous theoretical studies [18, 59]. The bottom CB of pure 1H-MoS_2 (Fig. 5 (a_1)) is mainly constituted of Mo 4d states, while the upper VB is composed of Mo 4d and S 3d states. This is one of the most important factors for the lower photocatalytic properties of pure 1H-MoS_2. For the Nb_{Mo}-1H-MoS_2 (Figs. 4 (b) and 5 (b)), the Nd 4d states appear in the upper VB. Thus the VB extends forward the CB and the band gap is decreased to 1.36 eV. Considering the Nb atom is one d-electron less than the Mo atom, the Nb atom will act as hole doping in the MoS_2 to form a p-type doping. More recently, an experimental study [51] shows Nb-substituted (concentration range 15%–25%) MoS_2 nanoparticles exhibit p-type character, which coincides with our theoretical calculation. Because of one electron removal, the effect on the Fermi energy below the valence band maximum (VBM) is notable which mainly originate from hybridized d orbitals of Nb and Mo (see Fig. 5 (b) and 5 (b_1)). The newly created defect states are rather delocalized and the charge excess spreads out up to the third nearest neighbor Mo atoms (Fig. 6 (a)). And also the

valence band (VB) looks sufficiently dispersive in our DFT band structure, and therefore the mobility of holes is expected to be rather large. On the other hand, some Nd 4d states are mixed with Mo 4d states in the CB of the Nb_{Mo}-1H-MoS_2. This is similar with the case of Nb doped into TiO_2 [60].

We also consider substitutional doping at the S site with elements taken from the halogen family, namely F, Cl, Br, and I (Figs. 4 (d) - (g) and 5 (d) - (g)). These systems are expected to act as a source of n-type doping for 1H-MoS_2, since they have one additional p-electron with respect to S. As a representative, we discuss in detail the results of F doping, since the other halogens present a similar electronic structure. For the F_S-1H-MoS_2 (Fig. 4 (d)), the upper VB still consists of Mo 4d and S 3d states, while the F 2p states hybride with Mo 4d states forming an occupied defect level below the CBM about 0.01 eV. These defect states originate from the hybridization between the F 2p and the Mo 4d states (see Fig. 5 (d) and 5 (d_1)). This is very similar to the case of F_S-ZnS [61]. As a result, the band gap of the F_S-1H-MoS_2 decreases to 1.481 eV from 1.652 eV. For other halogen dopants (Cl, Br, and I), similar results have been obtained (Figs. 4 and 5, Table 4).

It is very interesting that, different with the impurity states in the Nb_{Mo}-1H-MoS_2 and F_S-1H-MoS_2, there are no defect states in the $Nb_{Mo}F_S$-1H-MoS_2 (Fig. 4(c)). According to the results discussed above, this can be attributed to the charge compensated codoping because Nb_{Mo} and F_S are the donor-acceptor passivated dopants. Fig. 5 (c) and (c_1) show that the Nb 4d orbits would hybridize with S 3p states at the upper VB, while the hybridization of F 2p orbits with Nb 4d states is obvious at the bottom CB in the $Nb_{Mo}F_S$-1H-MoS_2. This hybridization will significantly strengthen the delocalization of Mo 4d, as shown in Fig. 6 (h). Furthermore, the resonance of the dopants states with host phase states leads to about 16.4% reduction of the energy gap (1.381 vs 1.652 eV), indicating codoping could effectively narrow the band gap, which is similar with the results of N+F-codoped TiO_2 [62]. The $Nb_{Mo}F_S$-1H-MoS_2 has a band structure similar to that of pure 1H-MoS_2. The results are very crucial for 1H-MoS_2 as a promising photocatalyst or photosensitizers for visible light in the heterogeneous semiconductor systems because this ensures improved charge carrier mobility in the codoped system. It should be pointed out that it is very difficult to precisely control the dopant sites in the fabricated samples. Thus, we

also consider another case: Nb and F atoms are separated each other. The calculated results show that the codopant sites have little influence on the calculated electronic structure, especially in the vicinity of Fermi level. More importantly, the calculated defect formation energy (-3.683 eV) indicates that Nb and F atoms are more inclined to form covalent bond when they are codoped into 1H-MoS_2. Therefore, we focus on the case that Nb atom is bonded to F atom in the 1H-MoS_2 in this work.

As is known, the photocatalytic activity is not only determined by the quantity of available photons, but also influenced by the quantum efficiency. During the photocatalytic reaction process, the recombination of photogenerated carriers easily occurs, thus decreasing the quantum efficiency. For the doped semiconductor photocatalysts, the impurity levels are either recombination or separation center of photogenerated carriers, depending on the property of impurity levels. The latter role of the impurity levels can be understood as follows. Under irradiation, the electron in the impurity level moves to the CBM by capturing a photon with enough energy, and a hole is left at the same time. Consequently, the electron at the VBM can leap into the impurity level by absorbing another appropriate photon. Thus, the hole in the impurity level is eliminated and a new hole forms in the VBM. As a result, the impurity level does not change, while an electron and a hole is generated in the CB and VB, respectively, indicating the separation of photogenerated carriers. But this process is largely determined by the mobility of the carriers, which can be indirectly characterized by the efficient masses of carriers. The efficient masses of carriers can be calculated using the equation, $m^*_{e/h} = \pm(\mathrm{h}/(2\pi^2))/(\mathrm{d}^2\mathrm{E}/\mathrm{dk}^2)^2$, where $m^*_{e/h}$ is the electron/hole efficient mass, *h* is the Planck constant, *k* is the wave vector and E is the energy of k. The positive and negative signs correspond to the electron and hole, respectively. Obviously, the effective mass depends on the curvature of the parabolic portions of the bands near the CBM and VBM. To obtain the m*, one has to calculate the coefficient of the second-order term in the quadratic fit of E(k). A large coefficient of the second-order term is corresponding to the low effective mass of the charge carrier, which implies a high mobility. Especially, a larger value of m^*_e/m^*_h, suggests a greater variation of the electron-hole mobility and thus a lower recombination rate of the electron-hole pairs.

Fig. 4 shows that the levels at the CBM and the VBM in pure 1H-MoS_2 and Nb_{Mo}-1H-MoS_2

are relatively dispersive, indicating the smaller value of m_e^*/m_h^*. Interestingly, the level just at the CBM in the $Nb_{Mo}F_S$-1H-MoS_2 is fairly flat, whereas that below the Fermi level is much dispersive, as is shown in Fig. 4 (c). Thus, the value of m_e^*/m_h^* in the $Nb_{Mo}F_S$-1H-MoS_2 is larger than that in pure 1H-MoS_2. The larger value of m_e^*/m_h^* also appears in NM_S-1H-MoS_2 (Fig. 4 (d) - (g)). The quantitative results from Fig. 4 indicate that the recombination rate of the electron-hole pairs in both $Nb_{Mo}F_S$-1H-MoS_2 and NM_S-1H-MoS_2 is low. On the other hand, Fig. 6 (c) - (f) show that the level just near the Fermi level in the NM_S-1H-MoS_2 are localized around the substitutional NM atom and three nearest Mo atoms. On the contrary, the lowest level of CB of the Nb_{Mo}-1H-MoS_2 is evenly distributed among the nearest six Mo atoms (Fig. 6 (a)), while the top level of VB on the nearest six Mo atoms and Nd atom (Fig. 6 (b)). The distribution of these states are one of the most basic and the most important factors for the enhanced photocatalytic activity of Nb_{Mo}-1H-MoS_2, as found in the experiment [51] .

For the $Nb_{Mo}F_S$-1H-MoS_2, the top level of VB is rather delocalized around the Nd atom (Fig. 6 (h)), while the level at the bottom CB, mainly consisted of Mo 4d states mixing with small F 2p oribtals, in the $Nb_{Mo}F_S$-1H-MoS_2 are distributed on the two Mo atoms connected with the dopant F, which can be clearly seen from Fig. 6 (g). This further indicates that the value of m_e^*/m_h^* in the $Nb_{Mo}F_S$-1H-MoS_2 is large, which is beneficial for the separation of the photogenerated charge carriers. Most importantly, the electrons in the VBM leap into the two Mo atoms by capturing a photon with enough energy (>1.38 eV). Therefore, the two Mo atoms connected with the dopant F become the active sites during the photocatalytic reaction process. This is, therefore, the first to reveal that the photocatalytic activity of the 1H-MoS_2 can be enhanced by the charge compensated codoping, such as Nb_{Mo} and F_S, because the catalytic activity of the codoped 1H-MoS_2 is not only derived from the under coordinated sulfur edge sites, but also from some new added active Mo sites in the basal planes which remain catalytically inert in the pure 1H-MoS_2.

4. Summary

In summary, a detailed first-principles calculation has been conducted to study the effect of $Nb_{Mo}F_S$ codoping on the structural and electronic properties of 1H-MoS_2 and compare the results with those for individual dopants. Although the Nd doping is able to enhance the absorption

intensity in the visible range, the localized impurity states introduced in the band gap would degrade the photocatalytic activity. Doping halogen element into 1H-MoS_2 leads to the introduction of occupied impurity states below the CB. After systematic exploring the origin of the appearance of the discrete states, we propose that these mid-gap states can be completely passivated by the charge compensated $Nb_{Mo}F_S$ codoping. This ensures the improved charge carrier mobility in the codoped system, thus helping extend the lifetime of the photogenerated charge carriers. Most importantly, this kind of charge compensated $Nb_{Mo}F_S$ codoping can add some new active Mo sites in the basal planes which remain catalytically inert in the pure 1H-MoS_2. The results elucidate the importance of charge compensated codoping in controllably tuning the band structure of 1H-MoS_2 to enhance its photocatalytic properties. This work is an example of heteroatom substitution in the case of 1H-MoS_2, opening up a wide range of possibilities including varying the electronic and optical behaviors of the 1H-MoS_2, in catalysis and in solar cells.

Acknowledgements

This work was supported by the Hunan Provincial Natural Science Foundation of China (Grant No. 12JJ3009), and Changsha Science and Technology Plan Projects (k1403067-11).

Reference

1. J. A. Wilson and A. D. Yoffe, Adv. Phys., 1969, **18**, 193-335.
2. K. S. Novoselov, K. S. Novoselov, D. Jiang, F. Schedin, T. J. Booth, and V. V. Khotkevich, Proc. Natl. Acad. Sci. U.S.A., 2005, **102**, 10451-10453.
3. A. K. Geim and K. S. Novoselov, Nat. Mater., 2007, **6**, 183-191.
4. C. H. Jin, F. Lin, K. Suenaga, and S. Iijima, Phys. Rev. Lett., 2009, **102**, 195505.
5. A. H. C. Neto and K. Novoselov, Rep. Prog. Phys., 2011, **74**, 082501.
6. X. R. Wang, Y. J. Ouyang, X. L. Li, H. L. Wang, and H. J. Dai, Phys. Rev. Lett., 2008, **100**, 206803.
7. S. Y. Zhou, G. H. Gweon, A. V. Fedorov, P. N. First, and W. A. De Heer, Nat. Mater., 2007, **6**, 770-775.
8. S. Adam, E. H. Hwang, V. M. Galitski, and S. Das Sarma, Proc. Natl. Acad. Sci. U.S.A., 2007, **104**, 18392-18397.
9. R. H. Friend and A. D. Yoffe, Adv. Phys., 1987, **36**, 1-94.
10. Q. H. Wang, K. Kalantar-Zadeh, A. Kis, J. N. Coleman, and M. S. Strano, Nat. Nanotechnol., 2012, **7**, 699-712.
11. T. Y. Chen, Y. H. Chang, C. L. Hsu, K. H. Wei, C. Y. Chiang, and L. J. Li, Int. J. Hydrogen Energy, 2013, **38**, 12302-12309.
12. M. Dallavalle, N. Saendig, and F. Zerbetto, Langmuir, 2012, **28**, 7393-7400.
13. C. Q. Feng, J. Ma, H. Li, R. Zeng, Z. P. Guo, and H. K. Liu, Mater. Res. Bull., 2009, **44**, 1811-1815.
14. K. K. Tiong and T. S. Shou, J. Phys. Condens. Matter, 2000, **12**, 5043-5052.
15. T. Korn, S. Heydrich, M. Hirmer, J. Schmutzler, and C. Schueller, Appl. Phys. Lett., 2011, **99**, 102109.
16. K. F. Mak, C. Lee, J. Hone, J. Shan, and T. F. Heinz, Phys. Rev. Lett., 2010, **105**, 136805.
17. A. Splendiani, L. Sun, Y. B. Zhang, T. S. Li, J. Kim, and C. Y. Chim, Nano Lett., 2010, **10**, 1271-1275.
18. S. Lebegue and O. Eriksson, Phys. Rev. B, 2009, **79**, 115409.
19. C. Ataca, M. Topsakal, E. Akturk, and S. Ciraci, J. Phys. Chem. C, 2011, **115**, 16354-16361.
20. Y. Ding, Y. L. Wang, J. Ni, L. Shi, S. Q. Shi, and W. H. Tang, Physica B, 2011, **406**, 2254-2260.
21. T. Cheiwchanchamnangij and W. R. L. Lambrecht, Phys. Rev. B, 2012, **85**, 205302.
22. Z. Y. Zhu , Y. C. Cheng, and U. Schwingenschloegl, Phys. Rev. B, 2011, **84**, 153402.
23. P. Johari and V.B. Shenoy, Acs Nano, 2012, **6**, 5449-5456.
24. Q. Yue, J. Kang, Z. Z. Shao, X. Zhang,S. L. Chang, and G. Wang, Phys. Lett. A, 2012, **376**, 1166-1170.
25. K. F. Mak, K. L. He, J. Shan, and T. F. Heinz, , Nat. Nanotechnol., 2012, **7**, 494-498.
26. J. N. Coleman, M. Lotya, A. O'Neill, S. D. Bergin, P. J. King, and U. Khan, Science, 2011,

331, 568-571.

27. Z. Y. Zeng, Z. Y. Yin,X. Huang, H. Li, Q. Y. He, and G. Lu, Angew. Chem. Int. Ed., 2011, **50**, 11093-11097.
28. A. Castellanos-Gomez, M. Barkelid, A. M. Goossens, V. E. Calado, and G. A. Steele, Nano Lett., 2012, **12**, 3187-3192.
29. J. G. He, K. C. Wu, R. J. Sa, Q. H. Li, and Y. Q. Wei, Appl. Phys. Lett., 2010, **96**, 082504.
30. C. Ataca and S. Ciraci, J. Phys. Chem. C, 2011, **115**, 13303-13311.
31. D. C. Sorescu, D.S. Sholl, and A.V. Cugini, J. Phys. Chem. B, 2004, **108**, 239-249.
32. M. Y. Sun, A. E. Nelson, and J. Adjaye, Catal. Today, 2005, **105**, 36-43.
33. M. Makarova, Y. Okawa, and M. Aono, J. Phys. Chem. C, 2012, **116**, 22411-22416.
34. Y. F. Li, D. H. Wu, Z. Zhou, C. R. Cabrera, and Z. F. Chen, J. Phys. Chem. Lett., 2012, **3**, 2221-2227.
35. E. W. K. Koh, C. H. Chiu, Y. K. Lim, Y. W. Zhang, and H. Pan, Int. J. Hydrogen Energy, 2012, **37**, 14323-14328.
36. N. Y. Topsoe, A. Tuxen, B. Hinnemann, J. V. Lauritsen, K. G. Knudsen, and F. Besenbacher, J. Catal., 2011, **279**, 337-351.
37. N. Singh, G. Jabbour, and U. Schwingenschloegl, Eur. Phys. J. B, 2012, **85**, 392.
38. D. James and T. Zubkov, J. Photochem. Photobiol. A, 2013, **262**, 45-51.
39. H. P. Komsa, J. Kotakoski, S. Kurasch, O. Lehtinen, U. Kaiser, and A. V. Krasheninnikov, Phys.Rev. Lett., 2012. **109**, 035503.
40. X. G. Yan, W. Q. Huang, G. F. Huang, L. Xu, S. Q. Zhan, Z. M. Yang, Z. Wan, P. Peng, Sci. Adv. Mater., 2014, **6**, 1221.
41. C. W. Tsai, M. H. Tu, C. J. Chen, T. F. Hung, R. S. Liu, and W. R. Liu, RSC Adv., 2011, **1**, 1349-1357.
42. X. L. Wei, M. S. Wang, Y. Bando, and D. Golberg, Acs Nano, 2011, **5**, 2916-2922.
43. L. Chen, C. S. Li, H. Tang, H. P. Li, X. J. Liu, and J. Meng, RSC Adv., 2014, **4**, 9573-9578.
44. Q. Yue, S. L. Chang, S. Q. Qin, and J. B. Li, Phys. Lett. A, 2013, **377**, 1362-1367.
45. Y. C. Cheng, Z. Y. Zhu, W. B. Mi, and Z. B. Guo, Phys. Rev. B, 2013, **87**, 100401.
46. V. V. Ivanovskaya, A. Zobelli, A. Gloter, N. Brun, V. Serin, and C. Colliex, Phys. Rev. B, 2008, **78**, 134104.
47. K. Dolui, I. Rungger, C. Das Pemmaraju, and S. Sanvito, Phys. Rev. B, 2013, **88**, 075420.
48. Y. Q. Gai, J. B. Li, S. S. Li, J. B. Xia, and S. H. Wei, Phys. Rev. Lett., 2009, **102**, 036402.
49. W. J. Yin, S. H. Wei, M. M. Al-Jassim, and Y. F. Yan, Phys. Rev. Lett., 2011, **106**, 066801.
50. C. P. Cheney, P. Vilmercati, E. W. Martin, M. Chiodi, L. Gavioli, and M. Regmi, Phys. Rev. Lett., 2014, **112**, 036404.
51. F. L. Deepak, H. Cohen, S. Cohen, Y. Feldman, R. Popovitz-Biro, and D. Azulay, J. Am. Chem. Soc., 2007, **129**, 12549-12562.
52. M. D. Segall, P. J. D. Lindan, M. J. Probert, C. J. Pickard, P. J. Hasnip, and S. J. Clark, J.

Phys. Condens. Matter, 2002, **14**, 2717-2744.

53. J. P. Perdew, K. Burke, and M. Ernzerhof, Phys. Rev. Lett., 1996, **77**, 3865-3868.
54. D. Vanderbilt, Phys. Rev. B, 1990, **41**, 7892-7895.
55. H. J. Monkhorst, and J. D. Pack, Phys. Rev. B, 1976, **13**, 5188-5192.
56. D. Yang, S. Jimenez Sandoval, W. M. R. Divigalpitiya, J. C. Irwin, and R. F. Frindt, Phys. Rev. B,1991, **43**, 12053-12056.
57. P. Joensen, E. D. Crozier, N. Alberding, and R. F. Frindt, J. Phys. C: Solid State Phys., 1987, **20**, 4043-4053.
58. D. Liu, Y. Guo, L. Fang, and J. Robertson, Appl. Phys. Lett., 2013, **103**, DOI: 10.1063/1.4824893.
59. Y. Li, Z. Zhou, S. B. Zhang, and Z. F. Chen, J. Am. Chem. Soc., 2008, **130**, 16739-16744.
60. S. G. Kim, M. J. Ju, I. T. Choi, W. S. Choi, H. J. Choi, and J. B. Baek, RSC Adv., 2013, **3**, 16380-16386.
61. H. Wan, L. Xu, W. Q. Huang, G. F. Huang, C. N. He, J. H. Zhou, and P. Peng, Appl. Phys. A, 2014, **116**, 741-750.
62. T. Z. Huang, S. Mao, J. M. Yu, Z. H. Wen, G. H. Lu, and J. H. Chen, RSC Adv., 2013, **3**, 16657-16664.

Table 1

Optimized cell parameters and bond lengths for pure and doped 1H-MoS_2

No.	Model[a]	Structure parameter (Å)		Bond length (Å)		
		a(=b)	c	NM-Mo	M-S	NM-M[b]
(a)	Nb_{Mo}	9.631	13.159		2.455	
(b)	F_S	9.511	13.202	2.275		
(c)	Cl_S	9.580	13.240	2.517		
(d)	Br_S	9.592	13.289	2.671		
(e)	I_S	9.598	13.392	2.879		
(f)	Nb_{Mo} F_S	9.530	13.276	2.220	2.449	2.224
					2.436(2)	
					2.432(2)	

[a] In pure 1H-MoS_2: a(=b)=9.542 Å, c=13.196 Å, the bond length Mo-S=2.409 Å

[b] NM and M means the substitutional nonmetal atoms and metal atom, respectivily.

Table 2

The population for pure and doped 1H-MoS_2

Model	Species	s	p	d	Total	Charge (e)
pure	S	1.86	4.16	--	6.02	-0.02
	Mo	2.46	6.45	5.04	13.95	0.05
Nb_{Mo}	Nb	2.43	6.28	3.94	12.66	0.34
	S	1.86	4.21	--	6.07	-0.07
	Mo	2.46	6.44	5.03	13.93	0.07
F_S	F	1.96	5.46	--	7.42	-0.42
	S	1.86	4.15	--	6.01	-0.01
	Mo	2.44	6.39	4.97	13.81	0.19
Cl_S	Cl	1.93	5.11	--	7.04	-0.04
	S	1.86	4.19	--	6.05	-0.05
	Mo	2.47	6.45	5.04	13.96	0.05
Br_S	Br	1.93	4.99	--	6.92	0.08
	S	1.86	4.19	--	6.05	-0.05
	Mo	2.46	6.47	5.05	13.98	0.02
I_S	I	1.93	4.81	--	6.73	0.27
	S	1.86	4.17	--	6.04	-0.04
	Mo	2.46	6.44	5.03	13.94	0.06
Nb_{Mo} F_S	F	1.95	5.47	--	7.42	-0.42
	S	1.86	4.22	--	6.08	-0.08
	Nb	2.41	6.24	3.87	12.52	0.48
	Mo	2.46	6.42	4.96	13.83	0.17

Table 3

Formation energy for different substitutional dopants in the 1H-MoS_2 for Mo-rich and for S-rich conditions

No.	Model	E_{form} (eV)	
		Mo-rich	S-rich
(a)	Nb_{Mo}	-0.25	-3.094
(b)	F_S	-2.318	-0.898
(c)	Cl_S	-0.102	1.318
(d)	Br_S	0.336	1.756
(e)	I_S	0.912	2.332
(f)	Nb_{Mo} F_S	-4.321	-5.743

Table 4

The E_v, E_c and E_g for pure and doped 1H-MoS_2

No.	Model	E_v (eV)	E_c (eV)	E_g (eV)
(a)	pure	0	1.652	1.652
(b)	Nb_{Mo}	0.097	1.457	1.360
(c)	F_S	-1.516	-0.035	1.481
(d)	Cl_S	-1.615	-0.115	1.500
(e)	Br_S	-1.565	-0.075	1.490
(f)	I_S	-1.470	0	1.470
(g)	Nb_{Mo} F_S	0	1.381	1.381

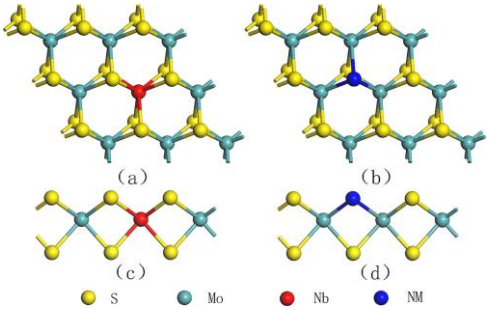

Fig. 1 Top (a, b) and side (c, d) views of the geometry structure for a (3×3) supercell of 1H-MoS_2 doped with impurities. The green, yellow, red, and blue spheres denote Mo, S, Nb, and NM atoms, respectively.

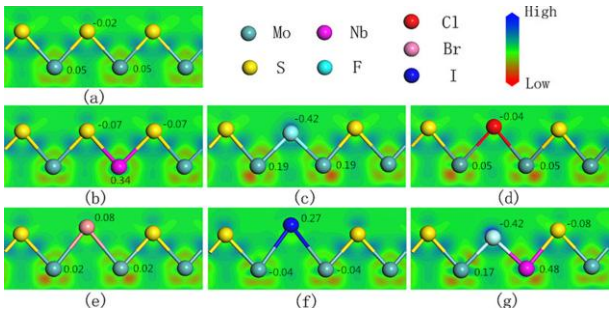

Fig. 2 Electron density difference maps for (a) pure, (b) Nb_{Mo}, (c) F_S, (d) Cl_S, (e) Br_S, (f) I_S, and (g) $Nb_{Mo}F_S$ doped 1H-MoS_2. The numbers are the population of atoms. The cross section is the (1 0 1) plane.

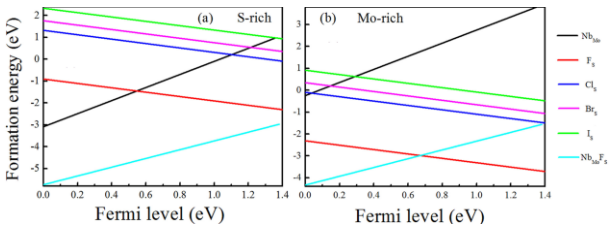

Fig. 3 Formation energies as a function of the Fermi level (referenced to the valence band maximum) of Nb_{Mo}, F_S, Cl_S, Br_S, I_S, and $Nb_{Mo}F_S$ doped in 1H-MoS_2, under (a) S-poor and (b) Mo-rich growth conditions.

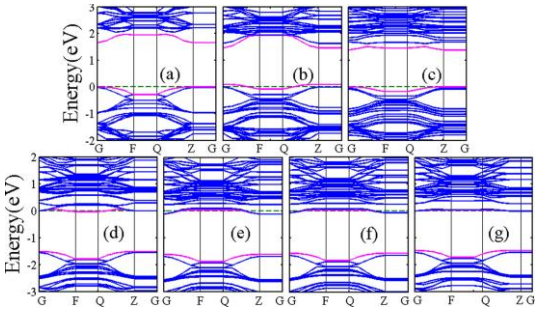

Fig. 4 Band structures of (a) pure, (b) Nb_{Mo}, (c) $Nb_{Mo}F_S$, (d) F_S, (e) Cl_S, (f) Br_S, and (g) I_S doped 1H-MoS_2. The Fermi level indicated by dashed line is set at 0 eV.

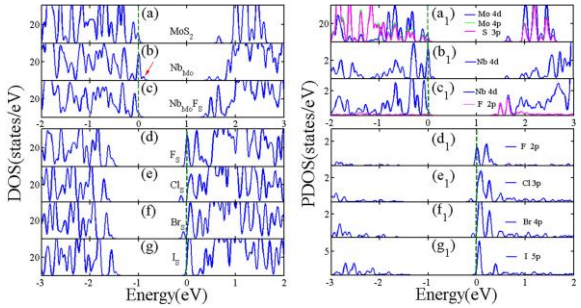

Fig. 5 DOS and PDOS of (a)-(a_1) pure, (b)-(b_1) Nb_{Mo}, (c)-(c_1) $Nb_{Mo}F_S$, (d)-(d_1) F_S, (e)-(e_1) Cl_S, (f)-(f_1) Br_S, and (g)-(g_1) I_S doped 1H-MoS_2. The Fermi level indicated by dashed line is set at 0 eV.

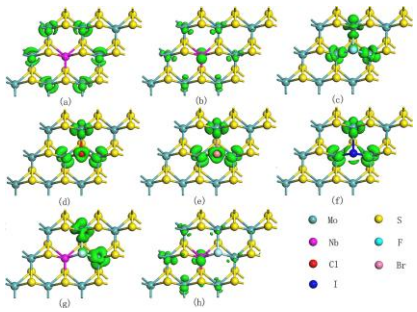

Fig. 6 Plots of the electron and hole density distributions with an isovalue of 0.04 e/Å^3: (a)-(b) and (g)-(h) are for the lowest level of CB and top level of VB of the Nb_{Mo}-MoS_2 and $Nb_{Mo}F_S$-MoS_2, respectively, (c)-(f) are for the first levels just above the Fermi level of F_S-MoS_2, Cl_S-MoS_2, Br_S-MoS_2, and I_S-MoS_2, respectively.